Cortical actin recovery at the immunological synapse leads to termination of lytic granule secretion in cytotoxic T lymphocytes

Alex T. Ritter[1,a,b], Senta M. Kapnick[1,c], Sricharan Murugesan[d], Pamela L. Schwartzberg[2,c], Gillian M. Griffiths[2,b], and Jennifer Lippincott-Schwartz[2,a]

[a]National Institute of Child Health and Development, National Institutes of Health, Bethesda, MD, 20892; [b]Cambridge Institute for Medical Research, Cambridge Biomedical Campus, University of Cambridge, Cambridge, CB2 0XY, United Kingdom; [c]National Human Genome Research Institute, National Institutes of Health, Bethesda, MD, 20892; [d]National Heart, Lung, and Blood Institute, National Institutes of Health, Bethesda, MD, 20892

J.L-S. present address: Howard Hughes Medical Institute-Janelia Research Campus, Ashburn, VA 20147

[1]These authors contributed equally to this work.

[2]Co-corresponding authors.

To whom correspondence may be addressed: pams@nhgri.nih.gov, gg305@cam.ac.uk, or lippincottschwartzj@janelia.hhmi.org

The authors declare no conflict of interest.

Author contributions: A.T.R. and S.M.K: research design, data collection and analysis, and writing the paper; S.M. assisted with data collection and analysis; P.L.S. research design, data analysis and writing the paper; G.M.G. and J.L.S research design, data review and writing the paper.

Figure 1

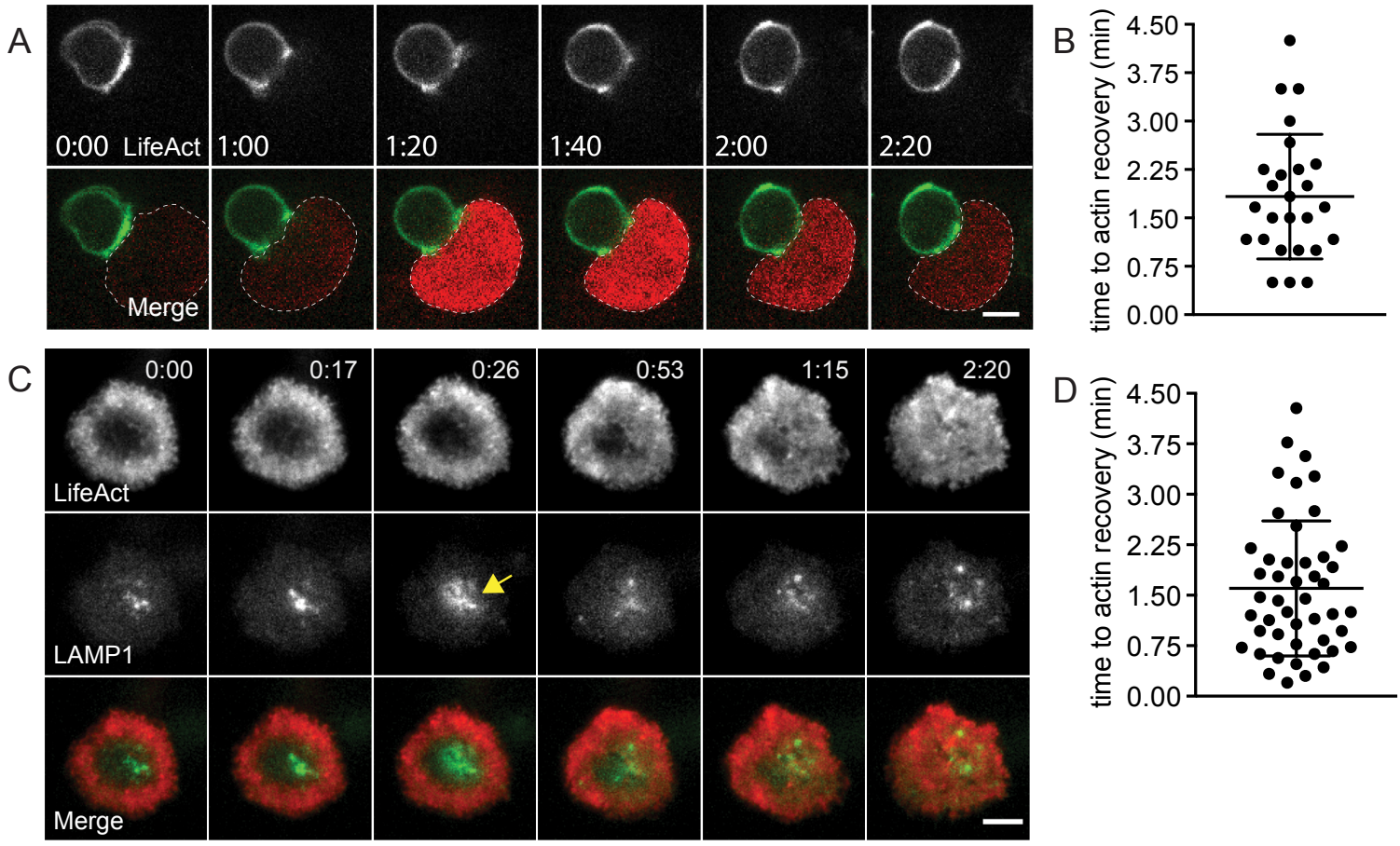
A
0:00 LifeAct
1:00
1:20
1:40
2:00
2:20
Merge
B
time to actin recovery (min)
4.50
3.75
3.00
2.25
1.50
0.75
0.00
C
0:00
0:17
0:26
0:53
1:15
2:20
LifeAct
LAMP1
Merge
D
time to actin recovery (min)
4.50
3.75
3.00
2.25
1.50
0.75
0.00

Figure 2

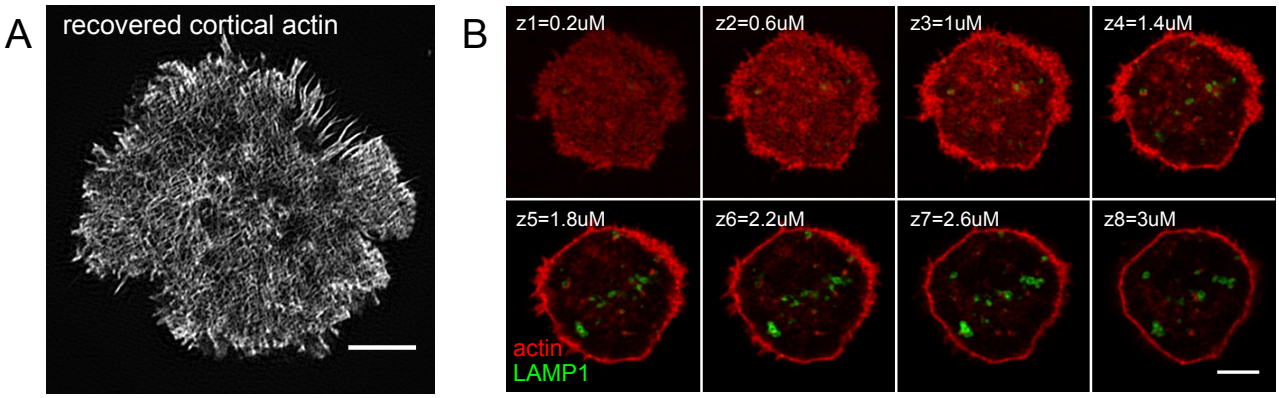
A
recovered cortical actin
B
z1=0.2uM
z2=0.6uM
z3=1uM
z4=1.4uM
z5=1.8uM
z6=2.2uM
z7=2.6uM
z8=3uM
actin
LAMP1

Figure 3

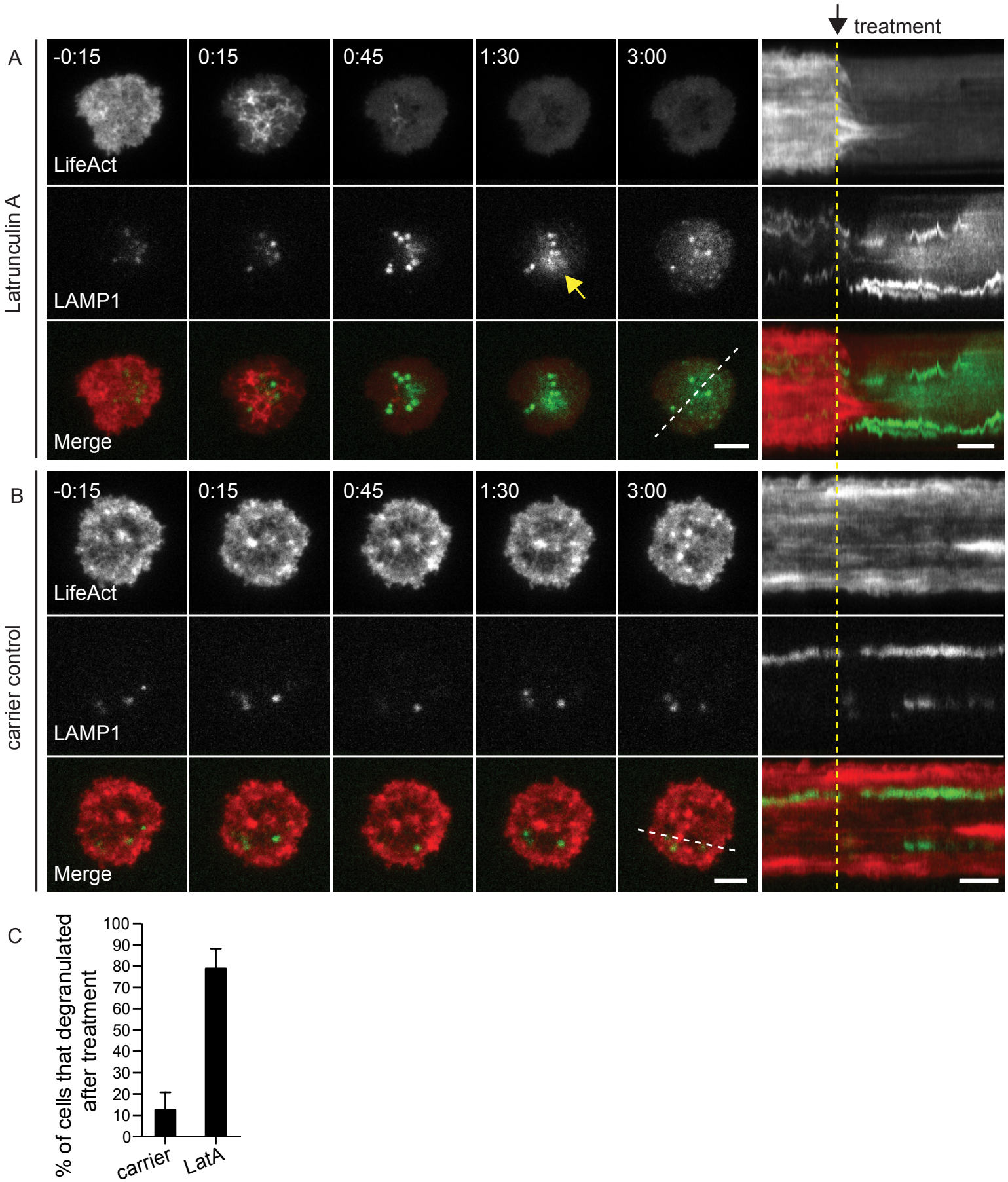
treatment
A
-0:15
0:15
0:45
1:30
3:00
LifeAct
LAMP1
Merge
Latrunculin A
B
-0:15
0:15
0:45
1:30
3:00
LifeAct
LAMP1
Merge
carrier control

C

% of cells that degranulated after treatment
100
90
80
70
60
50
40
30
20
10
0
carrier
LatA

Figure 4

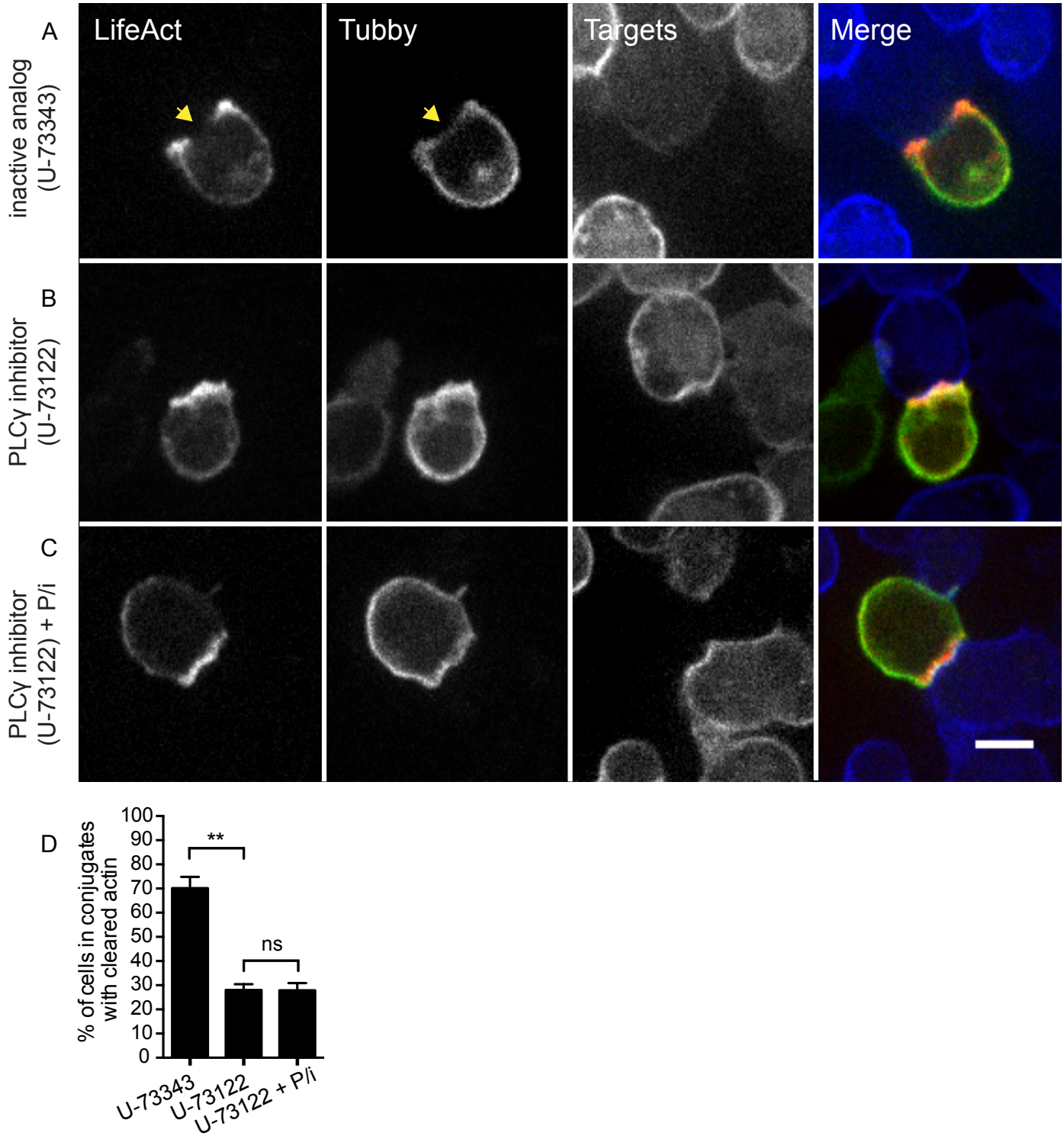
A
LifeAct
Tubby
Targets
Merge
inactive analog (U-73343)
B
PLCγ inhibitor (U-73122)
C
PLCγ inhibitor (U-73122) + P/i
D
% of cells in conjugates with cleared actin
100
90
80
70
60
50
40
30
20
10
0
**
ns
U-73343
U-73122
U-73122 + P/i

Figure 5

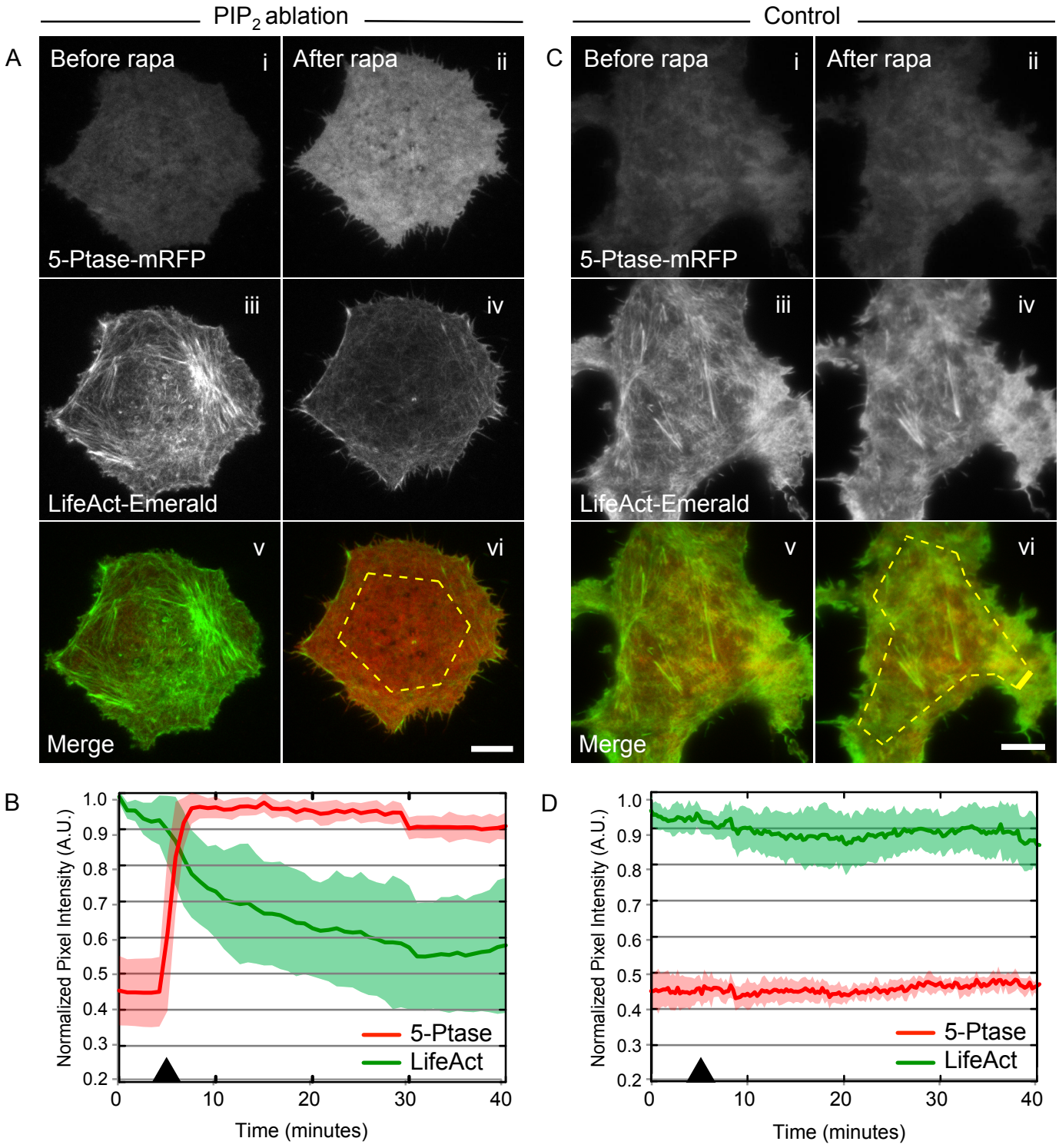
PIP2 ablation
Control
A
C
Before rapa
i
After rapa
ii
5-Ptase-mRFP
iii
iv
LifeAct-Emerald
v
vi
Merge
B
D
Normalized Pixel Intensity (A.U.)
1.0
0.9
0.8
0.7
0.6
0.5
0.4
0.3
0.2
0
10
20
30
40
Time (minutes)
5-Ptase
LifeAct

Figure 6

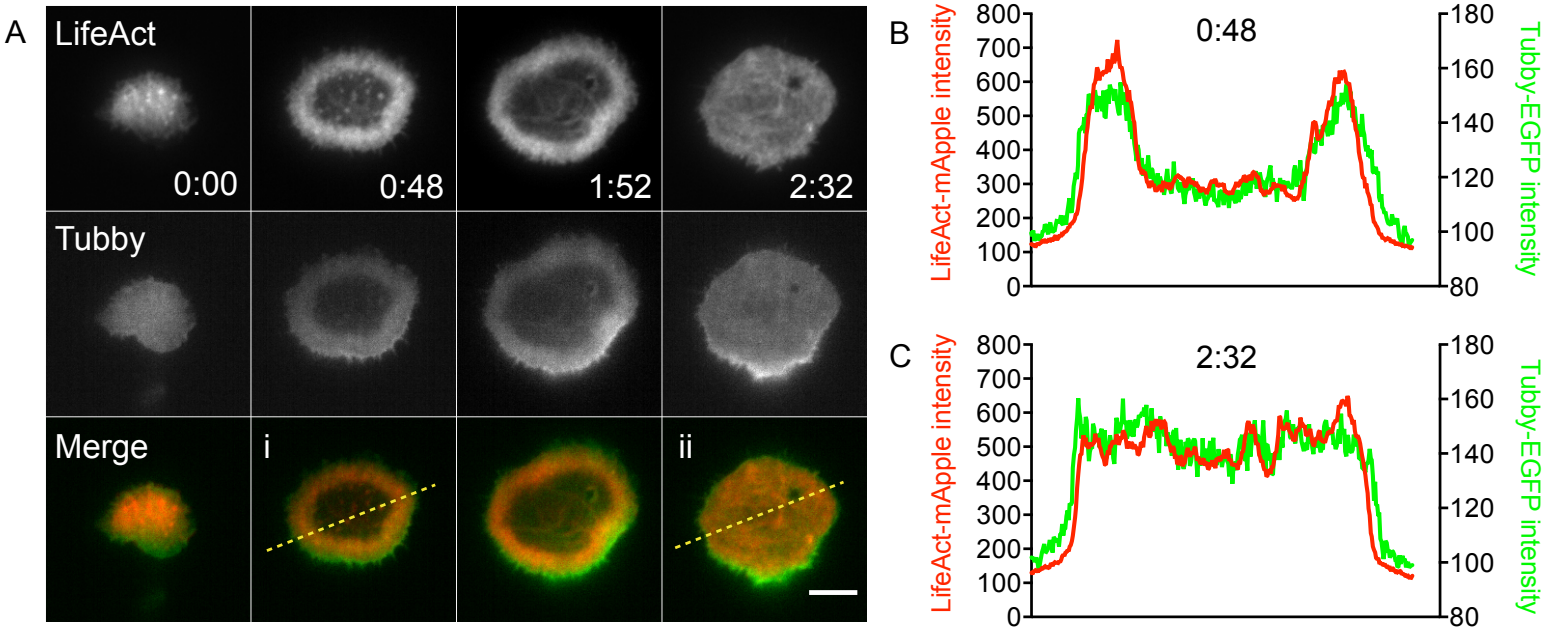
A
LifeAct
0:00
0:48
1:52
2:32
Tubby
Merge
i
ii
B
0:48
LifeAct-mApple intensity
Tubby-EGFP intensity
800
700
600
500
400
300
200
100
0
180
160
140
120
100
80
C
2:32
LifeAct-mApple intensity
Tubby-EGFP intensity

Figure 7

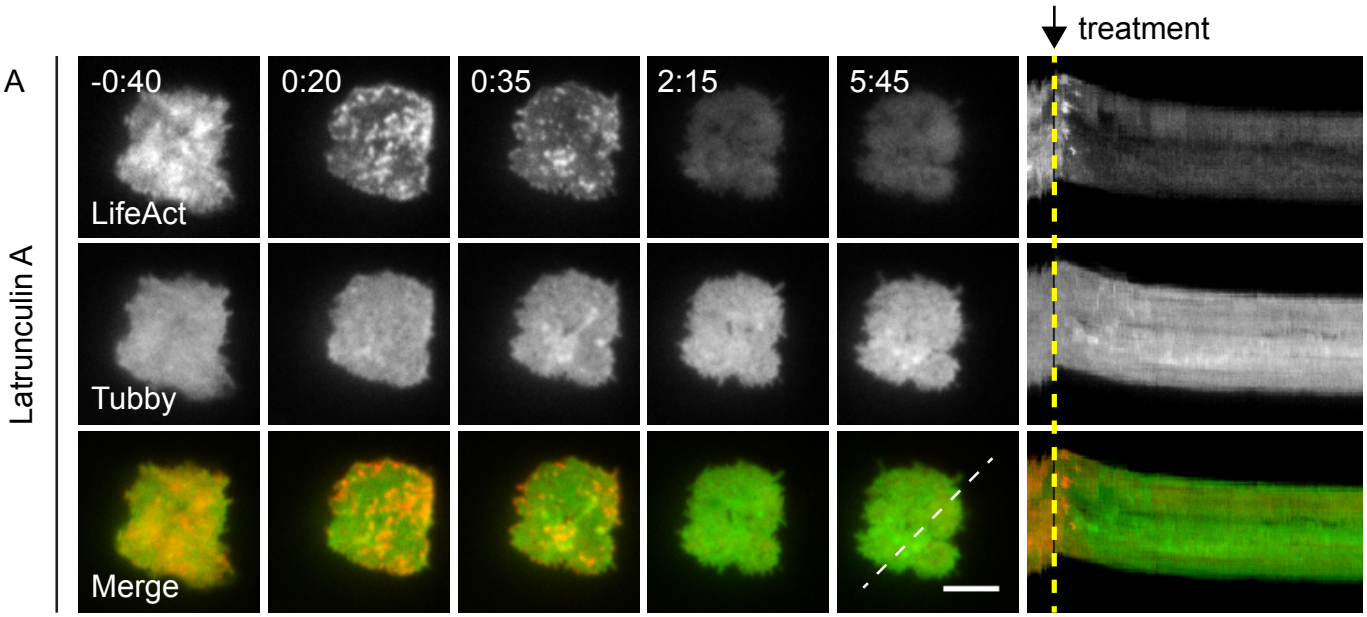
treatment
A
-0:40
0:20
0:35
2:15
5:45
LifeAct
Tubby
Merge
Latrunculin A

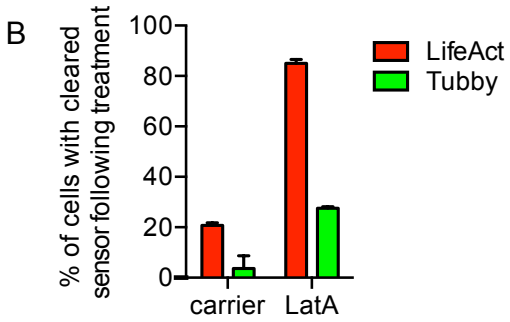
B
% of cells with cleared sensor following treatment
100
80
60
40
20
0
carrier
LatA
LifeAct
Tubby

Figure 8

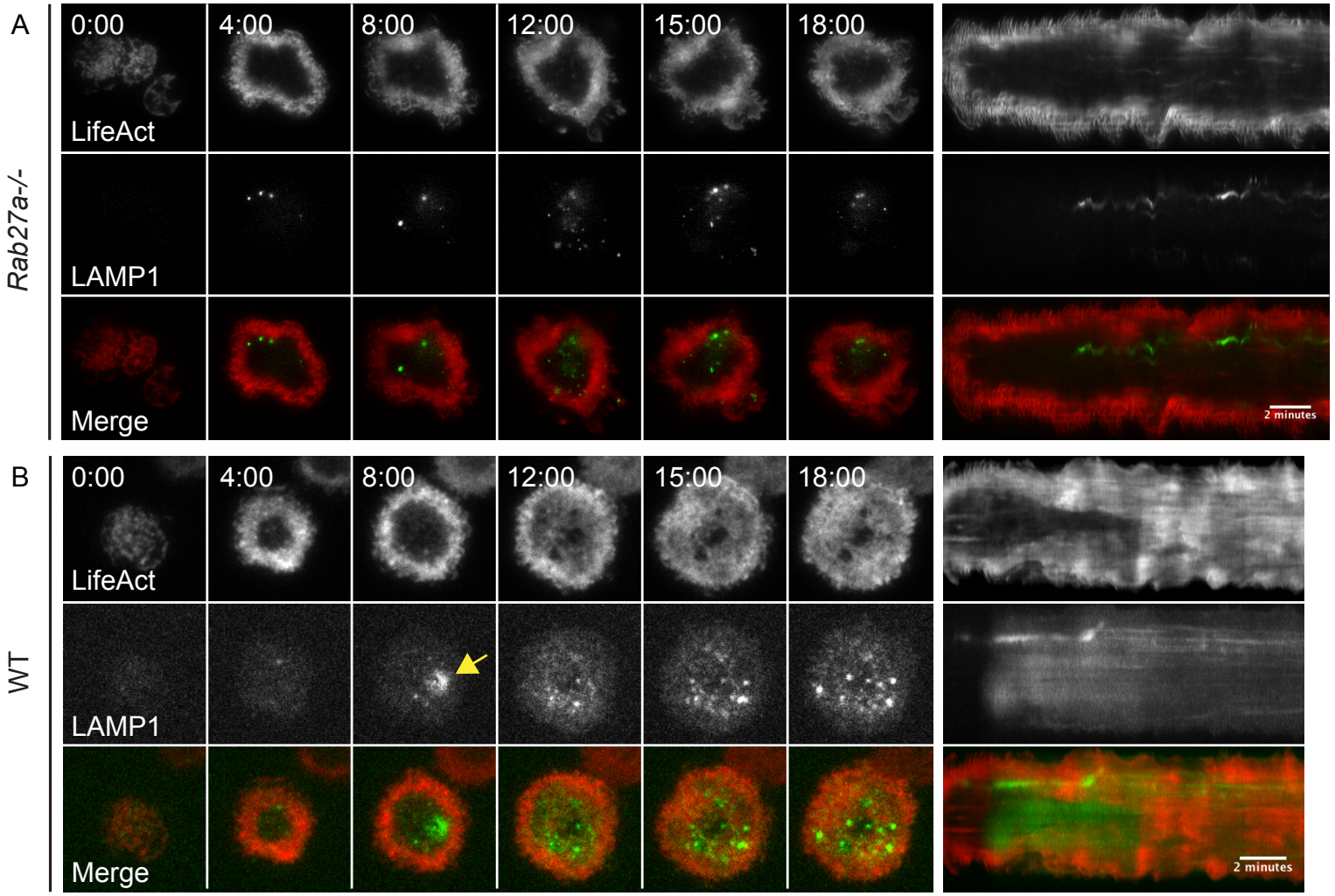
A
Rab27a-/-
0:00
4:00
8:00
12:00
15:00
18:00
LifeAct
LAMP1
Merge
2 minutes
B
WT
0:00
4:00
8:00
12:00
15:00
18:00
LifeAct
LAMP1
Merge
2 minutes

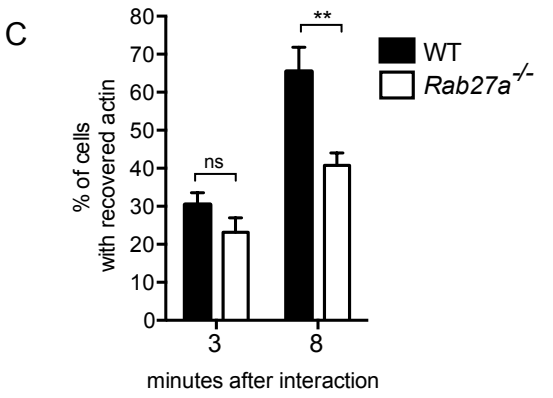
C
% of cells with recovered actin
80
70
60
50
40
30
20
10
0
ns
**
3
8
minutes after interaction
WT
Rab27a-/-

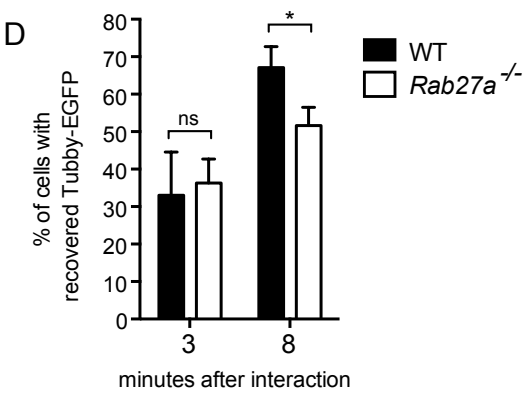
D
% of cells with recovered Tubby-EGFP
80
70
60
50
40
30
20
10
0
ns
*
3
8
minutes after interaction
WT
Rab27a-/-

Abstract

$CD8^+$ cytotoxic T-lymphocytes (CTLs) eliminate virally infected cells through directed secretion of specialized lytic granules. Because a single CTL can kill multiple targets, degranulation must be tightly regulated. However, how CTLs regulate the termination of granule secretion remains unclear. Previous work demonstrated that centralized actin depletion at the immune synapse precedes degranulation. Using a combination of live confocal, TIRF, and super-resolution microscopy, we now show that after granule fusion, actin recovers at the synapse and no further secretion is observed. Depolymerization of actin led to resumed granule secretion, suggesting recovered actin acts as a barrier preventing sustained degranulation. Furthermore, RAB27a-deficient CTLs, which do not secrete cytotoxic granules, failed to recover actin at the synapse, suggesting that RAB27a-mediated granule secretion is required for actin recovery. Finally, we show that both actin clearance and recovery correlated with synaptic PIP_2, and that alterations in PIP_2 at the immunological synapse regulate cortical actin in CTLs, providing a potential mechanism through which CTLs control cortical actin density. Our work provides insight into actin-related mechanisms regulating CTL secretion that may facilitate serial killing during immune responses.

Introduction

Cytotoxic $CD8^+$ T lymphocytes (CTLs) are critical for both the elimination of cells infected with intracellular pathogens and for the surveillance of tumors. CTLs carry out their cytolytic functions through the directed secretion of lytic granules, specialized lysosomes that contain perforin and granzymes that induce death of target cells. Because a single CTL is capable of killing multiple target cells during an immune response (1, 2), they are thought to act as "serial killers" (3). As such, CTLs need to tightly regulate secretion, both in order to kill only appropriate target cells on contact, and to facilitate their ability to carry out serial responses. Data suggest that each CTL releases only a small number of granules per productive killing outcome (4-6). However, how CTLs regulate both the initiation and the termination of granule secretion during an individual CTL:target interaction is still not completely understood.

A dense meshwork of cortical actin abuts the plasma membrane and envelops the cytosol of animal cells. Acute reduction of cortical actin density has been shown to regulate access of secretory granules to the plasma membrane and facilitate secretion in a number of cell types (7, 8). Notably, CTL recognition of a target is accompanied by rapid changes in cortical actin density resulting in a dramatic reduction of actin density at the interface between the CTL and its target (9, 10). Moreover, this reduction in cortical actin in CTLs is spatially and temporally correlated with the secretion of lytic granules (10). Conversely, elevated cortical actin density at the immunological synapse has been correlated with defective lytic granule secretion (11, 12). Nonetheless, the extent to which modulation of actin contributes to the regulation of secretion during later stages of T cell:target interactions and the termination of secretion is largely unknown.

To further explore the role of the cortical actin cytoskeleton in regulating both the initiation and the termination of secretion of cytolytic granules in CTLs, we used 3-dimensional, multicolor, live cell microscopy and total internal reflection fluorescence (TIRF) microscopy to directly examine the dynamics of cortical actin before, during, and after lytic granule secretion. Our results suggest that cortical actin density is tightly regulated to either permit or restrict access of lytic granules to the plasma membrane during target engagement. Furthermore, our data reveal a correlation between RAB27a-dependent secretion, the recovery of actin, and phosphatidylinositol 4,5-bisphosphate (PIP_2) at the synapse, suggesting that the distribution of PIP_2 in the membrane represents a potential mechanism through which CTLs regulate the density of cortical actin during cytolysis. Thus, by regulating the actin cytoskeleton, CTLs control both the initiation and termination of secretion, providing a potential mechanism to make them effective serial killers during an immune response.

Results

Cortical actin recovers at the synapse following lytic granule secretion

To evaluate cortical actin dynamics in the context of CTL cytolytic activity, we first employed live cell spinning disk confocal microscopy to follow actin during the entire course of CTL interactions with their targets. CTLs were derived from OT-I T cell receptor transgenic mice that recognize a peptide from Ovalbumin and were used in conjunction with peptide-pulsed targets expressing the Ca^{2+} indicator GCaMP6m, whose intensity directly correlates with intracellular calcium ion concentrations (1, 13-15). Previous work has shown that calcium increases are associated with very early loss of membrane integrity, as occurs in target cells after CTLs secrete their lytic granules containing perforin, which leads to the formation of pores in the target cell membrane (15-19). Thus, the increase in GCaMP6 intensity in the targets was used as a surrogate readout of productive lytic granule secretion by CTLs. To visualize actin in real time, CTLs were transfected with LifeAct-mEmerald, a fluorescently labeled actin-binding protein that allows visualization of polymerized actin in live cell imaging (20). Similar to previous results (6, 10), we saw a rapid reduction in cortical actin density at the synapse after CTL contact with target cells (Fig. 1A, 0:00 to 1:00 and Movie S1; Fig. S1 and Movie S2). This was followed by increased Ca^{2+} flux in targets (Fig. 1A, 1:20 and Movie S1), consistent with the effects of secretion of cytolytic granules by CTLs. Notably, once Ca^{2+} flux was observed in targets, cortical actin density recovered at the synapse in greater than 90% of the CTL:target conjugates, (Fig. 1A, 1:20 to 2:20), with a mean time of 1.83±0.96 minutes (mean±SD) following the initiation of GCaMP6 fluorescence (Fig. 1B). Thus, cortical actin appears to recover in CTLs after the directed secretion of cytolytic granules in cell conjugates.

Cortical actin recovery correlates with lytic granule secretion

To more fully evaluate the relationship between actin dynamics and lytic granule secretion, we applied a total internal reflection fluorescence (TIRF)-based imaging approach to T cell activation on a planar surface, which permits a rapid high-resolution view of the T cell synapse throughout stimulation, suitable for imaging granule fusion at the plasma membrane (21). To follow the fate of lytic granules, CTLs were co-transfected with LifeAct-mApple and LAMP1-EGFP, a marker for lytic granules (10). Cells were activated on anti-CD3-coated glass, allowing us to simultaneously visualize cortical actin density and lytic granule secretion over time. Upon engagement by anti-CD3, we observed a rapid reduction in cortical actin density at the center of the synapse, giving rise to a ring-like actin structure (Fig. 1C, first panel), as previously reported (6, 10). This was followed by the movement of lytic granules into the TIRF field (Fig. 1C and Movie S3). At various points after the appearance of granules, we observed the rapid diffusion of the LAMP1-EGFP fluorescent signal as the granule fused with the plasma membrane; this appeared as an explosion of fluorescence that rapidly diffused and disappeared (Fig. 1C, 0:26, and Movie S3). This phenomenon was distinct from lytic granules moving out of the TIRF field, which was not associated with diffusion of the EGFP signal in the plasma membrane. Notably, TIRF imaging confirmed that after degranulation, cortical actin density recovered across the immunological synapse (Fig. 1C, last panel).

To follow the kinetics of actin and degranulation, we focused on cells that were captured before actin had cleared, or early enough after clearance that lytic granules had not yet appeared in the TIRF field. Cells included in our analyses exhibited a contact interface that was large enough so that granule secretion events were sufficiently spatially separated for accurate quantification. Over time, 78% (51/65) of cells meeting this criteria degranulated, as indicated by

the diffusion of LAMP1-EGFP in the plasma membrane, with an average of 3.8±2.9 (mean±SD) granules fused per cell. Of the 51 cells in which we observed degranulation, 94% (48/51) recovered cortical actin across the synapse within the 20-minute window in which they were imaged in TIRF. In contrast, of the 14 cells that had not visibly degranulated, only 14% (2/14) recovered cortical actin within the same time period. The mean time to actin recovery following fusion of the last granule in TIRF was 1.6±1.0 minutes (mean±SD) (Fig. 1D), which closely approximates the time to actin recovery observed in our live-cell imaging (Fig. 1B). This recovery of cortical actin density in the center of the synapse contrasts with studies in Jurkat and $CD4^+$ cells, which do not secrete lytic granules, and in which actin rings are maintained for >40 minutes (21, 22). Interestingly, we noted that although granules could still be seen in the TIRF field behind the recovered cortical actin meshwork, once actin recovered, fusion was no longer observed. Thus, secretion only occurred during the period of actin clearance, actin recovery occurred after secretion, and once actin density recovered, secretion was no longer observed.

High resolution visualization of recovered actin at the synapse

To further evaluate the relationship between actin and lytic granules, we turned to structured illumination microscopy (SIM) in conjunction with a TIRF-based imaging system, (TIRF-SIM) (23), to visualize the recovered cortical actin network. OT-I CTLs expressing LAMP1-GFP were plated on anti-CD3-coated coverslips and fixed after 10 minutes, a time when most cells had already secreted lytic granules and recovered a dense cortical actin network across the synapse, as visualized by phalloidin staining (Fig. 2A). Notably, 3D reconstruction of SIM (3D-SIM) of phalloidin-stained CTLs expressing LAMP1-EGFP revealed that granules were localized behind the rich cortical actin meshwork (Fig. S2 and Movie S4). Granule positioning

behind the actin barrier was also evident in successive z stacks obtained using a confocal system fitted with an Airyscan module that increases resolution (Fig. 2B and Movie S5). These results raise the possibility that recovered cortical actin could serve as a physical barrier.

Cortical actin acts as a barrier to prevent secretion

The high resolution view of cortical actin at the synapse, in conjunction with the temporal correlation between actin recovery and the cessation of secretion, suggested to us that the recovered cortical actin could serve as a mechanism for regulating secretion in CTLs. To test this hypothesis, OT-I CTLs expressing LifeAct-mApple and LAMP1-EGFP were allowed to interact with anti-CD3-coated glass, secrete lytic granules, and recover cortical actin. At this point, cells were treated with a carrier control, or Latrunculin A (LatA) to depolymerize actin, and monitored using time lapse TIRF microscopy to observe the effects of treatment on lytic granule secretion. After treatment with LatA (Fig. 3A, 0:00 and Movie S6), we saw a rapid reduction in the intensity of cortical actin (0:15 to 0:45), demonstrating disassembly of the actin network. The reduction in cortical actin density was followed by lytic granule movement closer to the plasma membrane in the TIRF field, indicated by an increase in LAMP1-EGFP fluorescence intensity (Fig. 3A, 0:45 and Movie S6). Moreover, within one minute of the increase in EGFP intensity, lytic granule secretion was again observed at the plasma membrane, as indicated by the diffusion of EGFP in the TIRF plane (Fig. 3A, 1:30, and Movie S6). Evidence of this diffusion was also seen in the accompanying kymographs, which allowed visualization of fluorescence signal under a region of interest over time, in the form of a line drawn across the cell. In contrast, cortical actin density in carrier-treated cells remained relatively stable across the synapse, as demonstrated by the maintenance of the LifeAct-mApple fluorescent signal over time in

kymographs. While granules could be seen moving in and out of the TIRF field, the lack of LAMP1-EGFP diffusion into the plasma membrane throughout the kymograph and movies indicated that granule fusion had not occurred (Fig. 3B and Movie S7). Removal of the cortical actin barrier resulted in secretion in 78.9±9.4% of cells compared with secretion in only 12.5±8.2% of cells treated with a carrier control (Fig. 3C). These results suggest that recovered actin does indeed act as a barrier that effectively prevents sustained lytic granule secretion in CTLs.

Pharmacological inhibition of PLCγ1 inhibits actin clearance in CTLs

The regulation of secretion by the actin cytoskeleton raised the question of what factors contribute to the control of actin cytoskeletal dynamics at the CTL:target interface. One factor known to regulate cortical actin density is phosphatidylinositol 4,5-bisphosphate (PIP_2) (7, 24-26), which can bind and activate a variety of actin regulatory proteins (reviewed in (27)). We have previously described a correlation between the reduction in cortical actin density at the immunological synapse and decreased levels of PIP_2 (10).

To evaluate whether PIP_2 directly affects actin at the synapse, we first tried to alter levels of PIP_2 pharmacologically in CTLs. One of the key enzymes downstream of the TCR is Phospholipase–C gamma 1 (PLCγ1), which cleaves PIP_2 into IP_3 and DAG, two critical intermediates required for T cell activation that trigger Ca^{2+} flux and cell polarization changes, respectively (2, 28, 29). To address whether inhibition of PLCγ1 could modify local levels of its substrate, PIP_2, at the synapse, we co-transfected CTLs with LifeAct-mApple and a sensor expressing the PIP_2-binding domain of Tubby fused to EGFP (Tubby-EGFP) (30, 31). We then pretreated cells with either U-73122, an inhibitor of PLCγ1 activity, or U-73343, an inactive

analog (32), and allowed CTL:target conjugates to form before fixation. While cells treated with the inactive analog showed reduced Tubby-EGFP fluorescence (Fig. 4A), indicative of decreased PIP_2 at the synapse, U-73122-treated cells maintained uniform Tubby-EGFP fluorescence at the CTL:target interface (Fig. 4B). Strikingly, treatment with U-73122, but not the U-73343 control, also prevented clearance of cortical actin at the synapse (Fig.4A and B). To rule out that the effects of PLCγ1 inhibition on cortical actin dynamics were secondary to defective generation of the second messengers IP_3 and DAG, we allowed PLCγ inhibitor-treated CTLs to interact with target cells and then added phorbol 12-myristate 13-acetate (PMA) and ionomycin, which pharmacologically rescues DAG- and Ca^{2+} flux-mediated effects, respectively. Incubation with PMA and ionomycin in the presence of U-73122 failed to restore cortical actin clearance in CTLs (Fig. 4C), despite increasing expression of IFNγ and TNFα under the same conditions (Fig. S3). These results suggest that TCR-triggered PLCγ1 activation both decreases PIP_2 levels and contributes to the regulation of cortical actin density at the cytolytic synapse.

Acute PIP_2 ablation results in rapid disassembly of cortical actin meshwork

To more directly test whether altering PIP_2 levels affects cortical actin density, we employed an inducible system that allows for the selective ablation of PIP_2 from the membrane (33). Rapamycin treatment of cells transfected with components of this system induces dimerization of a membrane-tagged FRB-BFP protein with a cytosolic mRFP-FKBP12 fused to the catalytic domain of inositol lipid-5-phosphatase E (5-ptase), which converts $PI(4,5)P_2$ into PI4P, thereby recruiting the 5-ptase to the plasma membrane and effectively ablating PIP_2 there (Fig. S4A). This system has been used previously to look at the effects of PIP_2 depletion on

actin-mediated membrane ruffling (33) and clathrin-coated pit formation (34), but has not been used in conjunction with LifeAct to directly examine cortical actin integrity in real time.

To directly monitor the effects of acute modulation of PIP_2 using live cell imaging, we co-expressed the fluorescent reporters, Tubby-EGFP or LifeAct-mEmerald, with components of the inducible dimerization system. Because we were unable to obtain sufficient expression levels of these constructs in primary murine OT-I CTLs, we performed these experiments in Cos7 cells, where we could reproducibly co-express all components at adequate levels for visualization using TIRF. Addition of Rapamycin led to an immediate increase in the intensity of mRFP in the TIRF field, indicating that the 5-ptase was recruited to the plasma membrane (Fig. 5A and Supp. S4B). This was associated with a rapid reduction in the Tubby-EGFP signal, consistent with lower PIP_2 levels (Fig. S4B and Movie S8). Furthermore, in cells co-expressing LifeAct-mEmerald with the inducible system, we observed a rapid loss of cortical actin density following recruitment of the mRFP-tagged 5-ptase to the plasma membrane. (Figure 5A and 5B and Movie S9). In contrast, cells transfected with an FRB construct that failed to recruit the 5-ptase to the plasma membrane, did not exhibit changes in cortical actin (Figure 5C and 5D and Movie S10). Thus, acute manipulation of PIP_2 results in rapid changes in cortical actin density at the plasma membrane.

PIP_2 levels correlate with cortical actin recovery at the synapse

To evaluate whether there was a similar correlation between actin and PIP_2 during the recovery of cortical actin density at the synapse, we co-transfected CTLs with LifeAct-mApple and Tubby-EGFP (30, 31) and performed TIRF imaging on CTLs as they formed synapses on a planar activating surface. At early time points during interaction with anti-CD3-coated surfaces,

we observed that the reduction in cortical actin density at the center of the synapse was concurrent with a reduction in levels of PIP_2, consistent with our previous CTL:target conjugate imaging (Fig. 6A and Movie S11). Moreover, as cortical actin recovered at the synapse, we observed a concomitant recovery of Tubby-EGFP. Line scans confirmed the colocalization of fluorescence intensity for these two markers across the synapse at both early and late time points (Fig. 6Ai and ii, and 6B-C). These data suggest that PIP_2 levels not only correlate with the reduction in cortical actin density during early interactions, but additionally with the recovery of cortical actin across the synapse over time.

Finally, to confirm that PIP_2 recovery was not secondary to actin recovery, we treated CTLs after actin recovery with Latrunculin A as previously described in Fig. 3. Although treatment with Latrunculin A led to the rapid reduction of intensity of cortical actin, we did not observe changes in PIP_2 levels at the synapse (Fig. 7A and B and Movie S12, carrier controls in Fig. S5 and Movie S13). Thus, altering actin did not affect PIP_2 levels, while manipulation of PIP_2 led to dramatic changes in the cortical actin cytoskeleton. Together, these data suggest that PIP_2 acts upstream of actin to regulate the cortical actin meshwork.

Secretion-deficient *Rab27a*$^{ash/ash}$ CTLs show impaired actin recovery

In both live confocal and TIRF imaging of CTLs, we noted that cortical actin density recovered within two minutes following lytic granule secretion. These observations suggested to us that granule secretion itself may play a role in actin recovery. To test this hypothesis, we evaluated actin recovery in CTLs that were unable to secrete granules due to a mutation affecting RAB27a, a critical component of lytic granule docking machinery. Activation of both WT and RAB27A-deficient (*Rab27a*$^{ash/ash}$) cells on anti-CD3-coated glass led to a rapid reduction in

cortical actin density, followed shortly by the appearance of lytic granules within the TIRF field (Fig. 8A and B, and Movies S14 and S15). As expected, degranulation was not observed in *Rab27a*$^{ash/ash}$ CTLs, evidenced by a lack of diffusion of LAMP1-EGFP in TIRF (Fig. 8A), and confirmed in flow-based assays of LAMP1 cycling (data not shown). Remarkably, cortical actin density also did not recover in most RAB27a-deficient cells (Fig. 8A and Movie S14). Kymographic analyses confirmed that the area of reduced actin cortical density persisted throughout the duration of the 20 minute movie in the context of secretion-deficient CTLs when compared with WT CTLs, where cortical actin density recovered following secretion (Fig. 8A and B, right panels).

To more accurately quantitate actin recovery in the cell population, WT or *Rab27a*$^{ash/ash}$ CTLs were allowed to interact with anti-CD3-coated glass, and fixed at either an early (3 minutes, before granule secretion in WT CTLs) or a later time point (8 minutes, after granule secretion is expected to have occurred in most WT CTLs). Phalloidin staining of fixed cells revealed that while most WT CTLs had recovered actin across the synapse after eight minutes, secretion-deficient *Rab27a*$^{ash/ash}$ CTLs failed to recover actin as well as their WT counterparts (Fig. 8C). Similarly, evaluation of Tubby-EGFP in cells revealed that RAB27a-deficient CTLs did not fully recover PIP_2 across the synapse (Fig. 8D). Although we cannot rule out distinct effects of RAB27a, the observation that cortical actin does not recover in these cells suggests that lytic granule secretion might be a controlling mechanism that drives cortical actin recovery in CTLs. Taken together, our results support the idea that actin reorganization may be a critical step in both initiating and limiting CTL secretion.

Discussion

Studies of CTL:target interactions have revealed an exquisite regulation of cortical actin density at the immunological synapse, whereby cortical actin density is rapidly reduced specifically at interfaces between T cells and targets prior to lytic granule secretion (9, 10). Here, we have monitored cortical actin throughout the duration of TCR-triggered responses in the context of secretion and demonstrate that granule fusion in CTLs is consistently followed by the recovery of cortical actin across the immunological synapse. Our results suggest that recovered cortical actin may act as a barrier to limit granule secretion during a discrete CTL:target encounter, and furthermore, that recovery itself is triggered upon granule fusion, providing a mechanism that facilitates serial killing during an immune response. We also show that both clearance and recovery of cortical actin occurs concomitantly with complementary changes in PIP_2, suggesting that PIP_2 plays a role in tuning cortical actin density at the synapse in CTLs.

The role of actin in secretion has been studied in many cell types specializing in exocytosis, including NK cells (35-37), mast cells (7), pancreatic β cells (38), and adrenal chromaffin cells (39, 40). One model, known as the barrier model, suggests that the actin cortex acts to physically prevent vesicles from coming in close enough proximity to the plasma membrane for fusion to occur (38). This model is supported by evidence that actin prevents access of granules and fusion machinery to the plasma membrane in chromaffin cells (41). Our observations suggest that recovery of actin after granule fusion in CTLs may limit further access of lytic granules to the plasma membrane, thus preventing further secretion. This hypothesis is supported by our experiments showing that the removal of this cortical actin barrier using the actin depolymerization agent, Latrunculin A, resulted in resumed fusion of lytic granules. Thus, as in other cell types, cortical actin may form a barrier that blocks secretion in CTLs.

It has been suggested that actin plays an active role in lytic granule secretion, as lytic granules of NK cells appear preferentially localized in small areas of actin "hypodensity", but still within a meshwork of actin across the synapse (35, 36). In contrast, live cell imaging of CTL shows granule secretion occurs in an area of actin depletion across the synapse (9); whether remaining actin filaments might play a role in secretion remains to be seen. In this paper, we provide evidence that cortical actin density at the synapse recovers in CTLs and acts as a barrier to block access of granules to the plasma membrane, preventing sustained secretion. Whether dense actin networks also act as a barrier in NK cells is not known. It will also be interesting to see whether similar mechanisms for cortical actin regulation of secretion also hold true for directional versus non-directional secretion of other factors such as cytokines in T cells, which rely on similar stimuli but are found in different vesicular compartments.

The observation that cortical actin density recovered across the synapse during CTL:target interactions led us to explore what regulates actin dynamics in CTLs. Studies in macrophages report that the disassembly of actin around newly formed phagosomes correlated with the loss of PIP_2 (42). Actin cytoskeletal dynamics during phagocytosis in macrophages has been compared to immunological synapse formation in CTLs (43, 44) (and reviewed in (45)). Indeed, multiple reports suggest that T cells take up surface molecules from the membrane of cells with which they interact (6, 46). We therefore hypothesized that like in macrophages, PIP_2 has a role in regulating actin disassembly in CTLs. In agreement, we previously showed that loss of cortical actin density at the synapse correlates with a reduction in PIP_2 (10). Our study now further suggests that during TCR engagement, PIP_2 levels at the T cell synapse can be modulated by PLCγ1 activity. Although we cannot rule out other effects of the PLCγ1 inhibitor U-73122, treatment with PMA and Ionomycin failed to rescue actin clearance, suggesting these

observations were independent of DAG or Ca^{2+}-mediated effects. Indeed, PLCγ1 is recruited to and activated at TCR-triggered signaling complexes at the plasma membrane (47), making PLCγ1-mediated modulation of PIP_2 levels an attractive potential mechanism for regulating actin dynamics at the synapse. Moreover, our work now reveals that the recovery of actin also coincides with the recovery of PIP_2.

We further provide evidence that processes involved in granule secretion itself may trigger recovery of cortical actin at the synapse in CTLs. CTLs from ashen mice, which have a mutation leading to the loss of RAB27a, are unable to secrete lytic granules and kill target cells (48-50). In these CTLs, cortical actin density remained reduced at the immunological synapse long after most WT CTLs had degranulated and recovered their cortical actin. Although we cannot rule out a direct effect of RAB27a on actin, these results raise the possibility that secretion itself may play a role in the recovery of actin at the synapse in CTLs. Interestingly, mutations in *RAB27A* in humans lead to Griscelli syndrome type 2, a primary immunodeficiency associated with defective cytolysis and Hemophagocytic Lymphohistiocytosis, where IFNγ from hyperactivated CTLs leads to excessive activation of macrophages. Our observations raise the possibility that the hyperactivation of CTLs in Griscelli syndrome type 2 may result in part from effects of altered actin dynamics.

While we demonstrate here that secretion-impaired, RAB27a-deficient CTLs do not recover actin as well as secretion-competent CTLs, how granule fusion might trigger actin recovery at the synapse in CTLs is not clear. Fusion of lytic granules at the immunological synapse introduces new integral membrane proteins into the plasma membrane, including LAMP1 and LAMP2, which have large, heavily glycosylated ectodomains that could conceivably force apart the membranes between CTLs and their targets and thereby permit

inhibitory phosphatases such as CD45 access to abbreviate TCR signaling (51). In turn, this could allow the re-accumulation of PIP_2 through enzymatic activity or diffusion. Alternatively, fusion of granules may directly alter enzymes affecting phosphoinositide distribution or generation in the plasma membrane and thereby influence cortical actin density.

Based on our data, we propose a model in which the cortical actin meshwork acts as a barrier to that terminates secretion after CTL killing as it migrates around the body in search of a target. Upon CTL encounter with a target, TCR-triggering initiates a signaling cascade that leads to the recruitment of PLCγ1 to signaling complexes at the synapse, where it hydrolyzes PIP_2 in a localized fashion, thereby affecting actin regulatory factors. Polarization of the centrosome to the contact interface then delivers lytic granules to the immunological synapse in a region of reduced cortical actin density where they can efficiently fuse. Upon granule secretion the recovery of cortical actin across the synapse terminates further secretion. Whether this recovered actin then alters dynamics with target cells, allowing detachment to enable subsequent attack of new target cells remains an intriguing question. We propose that this secretion-induced cortical actin recovery offers a mechanism through which CTLs could limit secretion and preserve their capacity for serial killing during an immune response.

Materials and Methods

Mice

OT-I TCR transgenic (52) and C57BL/6 (Jackson Laboratories, Maine, USA) mice were maintained in a Specific Pathogen Free facility. Cells from *RAB27a*$^{ash/ash}$ mice were a generous gift from J. Hammer (NHLBI, NIH, Bethesda, MD). Cells were obtained from either male or female mice between 6-10 weeks of age. Animal husbandry and experiments were performed in accordance with protocols approved by the National Human Genome Research Institute Animal Use and Care Committee at the National Institutes of Health.

DNA constructs

DNA constructs used in this paper were generated as follows. Full length GCAMP6m (14) was cloned into the pMIG-R1 retroviral vector using BglII and EcoRI restriction sites to generate GCAMP6m-MIG-R1. Cloning of TagRFP-MEM-pMIG and Farnesyl-TagBFP2-pMIG were described previously (10). LifeAct-mApple, LifeAct-mEmerald, and mTagBFP2-Farnesyl-5 were obtained from M. Davidson (Florida State University, Tallahassee, FL). LAMP1-EGFP [human LAMP1 with C-terminal fluorescent protein tags] was a gift from G. Patterson (NIBIB, NIH, Bethesda, MD), and constructed exactly as described for PA-GFP-lgp120 (53). Constructs coding for the PH-binding domain of Tubby fused to EGFP (Tubby-EGFP), PM-FRB-mRFP, PM-FKBP-mRFP, and mRFP-5-ptase-FKBP12 were generous gifts from T. Balla (NICHD, NIH, Bethesda, MD) (31, 33). To produce PM-FRB-tagBFP2 and PM-FKBP-tagBFP2, the gene coding for tagBFP2 was removed from mTagBFP2-MAPTau-N10 using the restriction enzymes NotI and AgeI and exchanged with the gene coding for the mRFP fluorophore in the two PM-localized recruiter constructs.

Cell culture

To generate CTLs from OT-I mice, splenocytes were isolated and stimulated with 10nM $OVA_{257-264}$ peptide (AnaSpec, Fremont, CA, USA) in complete RPMI (RPMI 1640 plus 10% fetal calf serum (FCS), 2mM L-glutamine, 50U/mL penicillin/streptomycin, and 50μM β-mercaptoethanol). Following 3 days of stimulation, cells were resuspended in complete RPMI plus 10 IU/mL recombinant human IL-2 (rHIL-2), and seeded in fresh media at $0.5x10^6$ cells/mL every 48 hours. CTLs were used between 6 and 8 days after primary *in vitro* stimulation. To generate CTLs cells from WT and *Rab27a*$^{ash/ash}$ mice, purified $CD8^+$ T cells were activated using plate-bound 1μg/mL anti-CD3ε (clone 2C11) and 2μg/mL anti-CD28 (both from BioXCell, West Lebanon, NH, USA) for 48 hours in complete media. Following stimulation, cells were resuspended in fresh media + rhIL-2 and cultured for 4 days before use in assays. To generate EL4-GCAMP6m, retroviral supernatants from 293T cells transfected with the GCAMP6m-MIGR1 vector were used to transduce EL4 cells. Fluorescence activated cell sorting (FACS) was used to isolate the top 10% brightest expressing cells. COS7 cells and EL4 cell lines stably expressing Farnesyl-TagBFP2-pMIG and TagRFP-MEM-pMIG (described previously (10)), or GCAMP6m were maintained in DMEM with 10% FCS, 2mM L-glutamine, 50U/mL penicillin/streptomycin, and 50μM β-mercaptoethanol.

Live cell imaging

To prepare cells for live imaging, $5x10^6$ to $1x10^7$ *in vitro*-activated CTLs were transfected with 2.5μg DNA using the Mouse T Cell Nucleofector Kit (Lonza, Basel, Switzerland) 4-6 hours prior to imaging.

For spinning-disc confocal imaging of CTL-target interactions, specified targets were pulsed with 1μM OVA peptide for 1 hour at 37°C and washed once in serum-free DMEM (Gibco, Rockville, MD, USA). Targets were plated for 5 minutes in #1.5 glass 4- or 8-well imaging chambers (Lab-Tek, Rockville, MD, USA) previously coated with 0.5μg/ml murine ICAM-1/FC (R&D Systems, Minneapolis, MN, USA). Approximately $2x10^6$ CTLs were added drop wise to chambers containing targets, and serial confocal 1μm z stacks were acquired at 15-30-second intervals. Imaging began within five minutes of addition of the CTLs to each chamber. Images were acquired on either Nikon Ti3 microscope with a Yokogawa spinning-disk scan head (#CSU-X1, Yokogawa; Musashino-shi, Tokyo) and a Photometrics EM-CCD camera, or an Axio Observer Z1 microscope (Carl Zeiss Inc., Richmond, VA, USA) with a Zeiss Yokogawa Spinning Disk system and a Photometrics Evolve EM-CCD camera (Evolve 512, Tucson, AZ, USA).

For live TIRF microscopy of CTLs, #1.5 8-well glass imaging chambers (LabTek, Rockville, MD, USA) were cleaned and sonicated in 1M KOH for 15 min, coated with 0.01% poly-L-lysine (Sigma) for 15 min, washed with PBS, and then coated with 2.5μg anti-CD3ε (clone 2C11, BioXCell) in PBS for 1 hour at 37°C. PBS was replaced with warm RPMI (without phenol red) plus 5% FBS. CTLs (transfected as above) were then plated in chambers. Imaging began within two minutes of the addition of T cells to the chamber using Nikon Ti-E microscope using a 100x, Apo TIRF 1.49 NA oil-immersion objective (Nikon Instruments; Melville, NY, USA) with an iXon3 electron multiplying charged coupled device (EM-CCD, DU-897; Andor Technology, Belfast, Northern Ireland) or an Axio Observer Z1 microscope (Carl Zeiss Inc., Richmond, VA, USA) with TIRF fiber illuminator, oil immersion 100x TIRF objective, and using a cMOS camera (PCO Edge, Kelheim, Germany). For Latrunculin A experiments,

imaging began at least 15 minutes after addition of T cells to the imaging chamber. T cells were imaged for one to two minutes prior to the addition of Latrunculin A (1μM final concentration, Cayman Chemicals, Ann Arbor, MI, USA) or ethanol control. TIRF imaging continued another 10-15 minutes following treatment.

For the plasma membrane PIP_2 depletion experiments, COS7 cells were transfected with expression plasmids coding for PM-FRB-tagBFP2 (or PM-FKBP-tagBFP2) and mRFP-5ptase-FKBP12 at a 2:1 molar ratio. Depending on the experiment, cells were co-transfected with either Tubby-EGFP or Lifeact-mEmerald. Imaging was performed the following day performed in 8-well imaging chambers (LabTek) that were coated with 1:400 human Fibronectin (Millipore) for 30 minutes at room temperature. Transfected COS7 cells were trypsinized, washed and plated into the LabTek chambers 30 minutes prior to each experiment. The cells were imaged in TIRF for 5-10 minutes prior to the addition of a 3X stock of rapamycin (Sigma) to the chamber (final concentration: 100nM). The cells were monitored for another 40 minutes following addition of the drug to monitor the effects of 5-ptase recruitment to the PM. TIRF imaging was performed on a Nikon Ti3 TIRF microscope with a brick-and-block system to maintain a temperature of 37°C and atmosphere at 5% CO_2.

Fixed cell imaging in TIRF

For phalloidin experiments, WT or *Rab27a*$^{ash/ash}$ CTLs were plated in #1.5 4- or 8-well glass imaging chambers coated with 2.5μg anti-CD3ε, as described above. After 3 (early) or 8 (late) minutes following addition of CTLs to wells, media in chambers was replaced with 4% PFA for 10 minutes at room temperature, then cells were washed with PBS. Cells in chambers were then stained for 10 minutes with AlexaFluor 568 phalloidin (ThermoFisher Scientific,

Waltham, MA), and washed again with PBS. Samples were imaged using a 100x, Apo TIRF 1.49 NA oil-immersion objective with an iXon3 electron multiplying charged coupled device (EM-CCD, DU-897).

For LifeAct-mApple plus Tubby-EGFP imaging of fixed cells in TIRF, cells were co-transfected with LifeAct-mApple and Tubby-EGFP and added to #1.5 4- or 8-well glass imaging chambers coated with 2.5μg anti-CD3ε, as described above. After 3 or 8 minutes, cells in chambers were fixed with 4% PFA for 10 minutes at room temperature, washed with PBS, and imaged on an Axio Observer Z1 microscope with TIRF fiber illuminator, oil immersion 100x TIRF objective, and using a cMOS camera (PCO Edge).

Immunofluorescence confocal microscopy

Peptide-pulsed targets and transfected CTLs pretreated for 10 minutes at 37 C with indicated compounds (U-73122 or U-73343, final concentration 1μM, Sigma, St. Louis, MO, USA) were added drop wise to #1.5 4-well glass imaging chambers previously coated with 0.5μg/ml murine ICAM-1/FC and allowed to interact with targets for five minutes. Cells were then either fixed in 4% PFA for 10 minutes, or PMA (final concentration, 20ng/mL, Sigma, St. Louis, MO, USA) and ionomycin (final concentration, 1μg/mL, Sigma, St. Louis, MO, USA) were added for an additional five minutes, then fixed with 4% PFA. Cells in chambers were washed with PBS, and washed and left in PBS before imaging on an Axio Observer Z1 microscope or the Nikon Ti3 spinning disk microscopes described above.

For Airyscan imaging, confocal images were collected using a Zeiss LSM 880 confocal system fitted with an Airyscan module, mounted on an inverted Zeiss Axio Observer Z1 microscope with an oil immersion Plan-Apochromat 63x/1.40 DIC objective lens (Carl Zeiss

Inc., Thornwood, NY, USA). All images were acquired in Airyscan mode (Super-Resolution) using a 32-channel GaAsP-PMT detector. Excitation wavelengths of 488nm (2.2%) and 561nm (0.3%) were used for detection of LAMP1-EGFP and AlexaFluor 568 phalloidin; emissions were collected in a BP 420-480 + BP 495-620 filter, respectively. Zeiss ZEN 2.3 (black) software package was used for collection and post processing of the images. Airyscan processing was done using a 6.3 strength, 3D method.

Structured Illumination Microscopy (SIM)

WT CTLs previously transfected with LAMP1-EGFP were added to #1.5 8-well glass chambers coated with 2.5μg anti-CD3ε, as described. After 10 minutes at 37 C, cells were fixed with 4% PFA, and stained with AlexaFluor 568 phalloidin for 10 minutes at room temperature, washed and maintained in PBS. 3D-SIM of these cells was performed on a GE DeltaVision OMX SR (Applied Precision Ltd.; GE Healthcare) equipped with a 60× 1.42 NA objective (Olympus). Raw data from 3-6 micron Z-stacks were reconstructed using Softworx (Applied Precision Ltd.; GE Healthcare) and values between 0.001-0.003 for the Wiener filter constant.

Image acquisition and analysis software, and statistics

Image acquisition on systems was controlled using Nikon NIS-Elements, Zeiss Zen Blue Software, and OMX Master Control Software AcquireSR. Data were analyzed with Imaris Scientific Image Processing and Analysis Software (Bitplane Scientific Software, Zurich, Switzerland) and ImageJ (NIH, Bethesda, MD, USA) software. All statistical analyses were performed using Microsoft Excel or Graph Pad Prism software. P values less than 0.05 were considered statistically significant.

Acknowledgments

The authors would like to thank members of the Griffiths, Schwartzberg, and Lippincott-Schwartz laboratories, including A. Weigel and C. Obara (HHMI-Janelia Research Campus), and Y. Asano (CIMR) for assistance with data analysis, Y. Asano, C. Gawden-Bone, and J.C. Stinchcombe (CIMR), L. Samelson (NCI) and T. Balla (NICHD) for critical reading of the manuscript and helpful discussions, S. Wincovitch (NHGRI) for assistance with imaging, T. Balla (NICHD) and M.W. Davidson (deceased, formerly of FSU) for DNA constructs, and J. Hammer (NHLBI) for *RAB27a*$^{ash/ash}$ cells and helpful discussion. This work was supported by funding from the Wellcome Trust ([103930] and [100140], GMG and ATR), and intramural funding of NICHD (JLS and ATR), NHGRI (SMK and PLS) and NHLBI (SM), National Institutes of Health, Bethesda, MD.

References

1. Halle S*, et al.* (2016) In vivo killing capacity of cytotoxic T cells Is limited and involves dynamic interactions and T cell cooperativity. *Immunity* 44(2):233-245.

2. Quann EJ, Merino E, Furuta T, & Huse M (2009) Localized diacylglycerol drives the polarization of the microtubule-organizing center in T cells. *Nat Immunol* 10(6):627-635.

3. Bossi G*, et al.* (2002) The secretory synapse: the secrets of a serial killer. *Immunol Rev* 189:152-160.

4. Ming M, Schirra C, Becherer U, Stevens DR, & Rettig J (2015) Behavior and Properties of Mature Lytic Granules at the Immunological Synapse of Human Cytotoxic T Lymphocytes. *PLoS One* 10(8):e0135994.

5. Lyubchenko TA, Wurth GA, & Zweifach A (2001) Role of calcium influx in cytotoxic T lymphocyte lytic granule exocytosis during target cell killing. *Immunity* 15(5):847-859.

6. Stinchcombe JC, Bossi G, Booth S, & Griffiths GM (2001) The immunological synapse of CTL contains a secretory domain and membrane bridges. *Immunity* 15(5):751-761.

7. Wollman R & Meyer T (2012) Coordinated oscillations in cortical actin and Ca2+ correlate with cycles of vesicle secretion. *Nat Cell Biol* 14(12):1261-1269.

8. Porat-Shliom N, Milberg O, Masedunskas A, & Weigert R (2013) Multiple roles for the actin cytoskeleton during regulated exocytosis. *Cell Mol Life Sci* 70(12):2099-2121.

9. Stinchcombe JC, Majorovits E, Bossi G, Fuller S, & Griffiths GM (2006) Centrosome polarization delivers secretory granules to the immunological synapse. *Nature* 443(7110):462-465.

10. Ritter AT*, et al.* (2015) Actin depletion initiates events leading to granule secretion at the immunological synapse. *Immunity* 42(5):864-876.

11. Tsun A*, et al.* (2011) Centrosome docking at the immunological synapse is controlled by Lck signaling. *J Cell Biol* 192(4):663-674.

12. Zhao F, Cannons JL, Dutta M, Griffiths GM, & Schwartzberg PL (2012) Positive and Negative Signaling through SLAM Receptors Regulate Synapse Organization and Thresholds of Cytolysis. *Immunity* 36(6):1003-1016.

13. Keefe D*, et al.* (2005) Perforin triggers a plasma membrane-repair response that facilitates CTL induction of apoptosis. *Immunity* 23(3):249-262.

14. Chen TW*, et al.* (2013) Ultrasensitive fluorescent proteins for imaging neuronal activity. *Nature* 499(7458):295-300.

15. Sneller MC, *et al.* (1997) Clinical, immunologic, and genetic features of an autoimmune lymphoproliferative syndrome associated with abnormal lymphocyte apoptosis. *Blood* 89(4):1341-1348.

16. Dennert G & Podack ER (1983) Cytolysis by H-2-specific T killer cells. Assembly of tubular complexes on target membranes. *J Exp Med* 157(5):1483-1495.

17. Masson D & Tschopp J (1985) Isolation of a lytic, pore-forming protein (perforin) from cytolytic T-lymphocytes. *J Biol Chem* 260(16):9069-9072.

18. Henkart P, *et al.* (1985) The role of cytoplasmic granules in cytotoxicity by large granular lymphocytes and cytotoxic T lymphocytes. *Adv Exp Med Biol* 184:121-138.

19. Poenie M & Epel D (1987) Ultrastructural localization of intracellular calcium stores by a new cytochemical method. *J Histochem Cytochem* 35(9):939-956.

20. Riedl J, *et al.* (2008) Lifeact: a versatile marker to visualize F-actin. *Nat Methods* 5(7):605-607.

21. Bunnell SC, Kapoor V, Trible RP, Zhang W, & Samelson LE (2001) Dynamic actin polymerization drives T cell receptor-induced spreading: a role for the signal transduction adaptor LAT. *Immunity* 14(3):315-329.

22. Barda-Saad M, *et al.* (2005) Dynamic molecular interactions linking the T cell antigen receptor to the actin cytoskeleton. *Nat Immunol* 6(1):80-89.

23. Li D, *et al.* (2015) ADVANCED IMAGING. Extended-resolution structured illumination imaging of endocytic and cytoskeletal dynamics. *Science* 349(6251):aab3500.

24. Shibasaki Y, *et al.* (1997) Massive actin polymerization induced by phosphatidylinositol-4-phosphate 5-kinase in vivo. *J Biol Chem* 272(12):7578-7581.

25. Gilmore AP & Burridge K (1996) Regulation of vinculin binding to talin and actin by phosphatidyl-inositol-4-5-bisphosphate. *Nature* 381(6582):531-535.

26. Apgar JR (1995) Activation of protein kinase C in rat basophilic leukemia cells stimulates increased production of phosphatidylinositol 4-phosphate and phosphatidylinositol 4,5-bisphosphate: correlation with actin polymerization. *Mol Biol Cell* 6(1):97-108.

27. Yin HL & Janmey PA (2003) Phosphoinositide regulation of the actin cytoskeleton. *Annu Rev Physiol* 65:761-789.

28. Weiss A & Samelson LE (2003) T-lymphocyte activation. *Fundamental Immunology*, ed Paul WE (Lippincott-Raven, New York), pp 321-363.

29. Rhee SG (2001) Regulation of phosphoinositide-specific phospholipase C. *Annu Rev Biochem* 70:281-312.

30. Balla T & Varnai P (2009) Visualization of cellular phosphoinositide pools with GFP-fused protein-domains. *Curr Protoc Cell Biol* Chapter 24:Unit 24 24.

31. Szentpetery Z, Balla A, Kim YJ, Lemmon MA, & Balla T (2009) Live cell imaging with protein domains capable of recognizing phosphatidylinositol 4,5-bisphosphate; a comparative study. *BMC Cell Biol* 10:67.

32. Bleasdale JE, *et al.* (1989) Inhibition of phospholipase C dependent processes by U-73122. *Adv Prostaglandin Thromboxane Leukot Res* 19:590-593.

33. Varnai P, Thyagarajan B, Rohacs T, & Balla T (2006) Rapidly inducible changes in phosphatidylinositol 4,5-bisphosphate levels influence multiple regulatory functions of the lipid in intact living cells. *J Cell Biol* 175(3):377-382.

34. Zoncu R, *et al.* (2007) Loss of endocytic clathrin-coated pits upon acute depletion of phosphatidylinositol 4,5-bisphosphate. *Proc Natl Acad Sci U S A* 104(10):3793-3798.

35. Clark RH, *et al.* (2003) Adaptor protein 3-dependent microtubule-mediated movement of lytic granules to the immunological synapse. *Nat Immunol* 4(11):1111-1120.

36. Rak GD, Mace EM, Banerjee PP, Svitkina T, & Orange JS (2011) Natural killer cell lytic granule secretion occurs through a pervasive actin network at the immune synapse. *PLoS Biol* 9(9):e1001151.

37. Brown AC, *et al.* (2011) Remodelling of cortical actin where lytic granules dock at natural killer cell immune synapses revealed by super-resolution microscopy. *PLoS Biol* 9(9):e1001152.

38. Orci L, Gabbay KH, & Malaisse WJ (1972) Pancreatic beta-cell web: its possible role in insulin secretion. *Science* 175(4026):1128-1130.

39. Giner D, *et al.* (2005) Real-time dynamics of the F-actin cytoskeleton during secretion from chromaffin cells. *J Cell Sci* 118(Pt 13):2871-2880.

40. Villanueva J, *et al.* (2012) The F-actin cortex in chromaffin granule dynamics and fusion: a minireview. *J Mol Neurosci* 48(2):323-327.

41. Torregrosa-Hetland CJ, *et al.* (2011) The F-actin cortical network is a major factor influencing the organization of the secretory machinery in chromaffin cells. *J Cell Sci* 124(Pt 5):727-734.

42. Scott CC, *et al.* (2005) Phosphatidylinositol-4,5-bisphosphate hydrolysis directs actin remodeling during phagocytosis. *J Cell Biol* 169(1):139-149.

43. Martinez-Martin N, *et al.* (2011) T cell receptor internalization from the immunological synapse is mediated by TC21 and RhoG GTPase-dependent phagocytosis. *Immunity* 35(2):208-222.

44. Goodridge HS, *et al.* (2011) Activation of the innate immune receptor Dectin-1 upon formation of a 'phagocytic synapse'. *Nature* 472(7344):471-475.

45. Niedergang F, Di Bartolo V, & Alcover A (2016) Comparative Anatomy of Phagocytic and Immunological Synapses. *Front Immunol* 7:18.

46. Huang JF, *et al.* (1999) TCR-Mediated internalization of peptide-MHC complexes acquired by T cells. *Science* 286(5441):952-954.

47. Braiman A, Barda-Saad M, Sommers CL, & Samelson LE (2006) Recruitment and activation of PLCgamma1 in T cells: a new insight into old domains. *Embo J* 25(4):774-784.

48. Wilson SM, *et al.* (2000) A mutation in Rab27a causes the vesicle transport defects observed in ashen mice. *Proc Natl Acad Sci U S A* 97(14):7933-7938.

49. Stinchcombe JC, *et al.* (2001) Rab27a is required for regulated secretion in cytotoxic T lymphocytes. *J Cell Biol* 152(4):825-834.

50. Haddad EK, Wu X, Hammer JA, 3rd, & Henkart PA (2001) Defective granule exocytosis in Rab27a-deficient lymphocytes from Ashen mice. *J Cell Biol* 152(4):835-842.

51. Davis SJ & van der Merwe PA (2006) The kinetic-segregation model: TCR triggering and beyond. *Nat Immunol* 7(8):803-809.

52. Hogquist KA, *et al.* (1994) T cell receptor antagonist peptides induce positive selection. *Cell* 76(1):17-27.

53. Patterson GH & Lippincott-Schwartz J (2002) A photoactivatable GFP for selective photolabeling of proteins and cells. *Science* 297(5588):1873-1877.

Figure Legends

Fig. 1. Cortical actin recovery at the CTL synapse follows lytic granule secretion. (A) Spinning disk confocal time lapse images of an OT-I CTL expressing LifeAct-mApple (pseudocolored in green) in conjugate with an EL4 target cell expressing GCaMP6m pulsed with 1μM OVA_{257-26} (highlighted by dotted line). Images showing signal from the LifeAct channel in a single slice correspond to the center of the synapse and are shown in gray scale (top row). GCaMP6m fluorescence (red) corresponds to an increase in Ca^{2+} in the target cell. Data are representative from N=26 cells from 5 independent experiments. Time in figure is shown in minutes:seconds; scale bar = 5μm. (B) Graph represents time to actin recovery in CTLs following initiation of GCaMP6m fluorescence in the targets. (C) TIRF images of an OT-I CTL expressing LifeAct-mApple (red) and LAMP1-EGFP (green) degranulating on anti-CD3-coated glass surfaces (merge, bottom row). Top row displays signal from the LifeAct channel and middle row from the LAMP1-EGFP channel, shown in gray scale. Degranulation event in the middle row is highlighted by a yellow arrowhead. Data are representative of N=65 cells from 9 independent experiments. Time in figure is shown in minutes:seconds; scale bar = 5μm. (D) Graph represents time to actin recovery in CTLs following fusion of the last granule in TIRF movies.

Fig. 2. High-resolution visualization of recovered actin at the synapse. (A) Representative TIRF SIM image of recovered cortical actin in a phalloidin-stained OT-I CTL fixed after 10 minutes following stimulation on anti-CD3-coated glass surfaces. Scale bar = 3μm. (B) Successive 0.4μm z stack images obtained via Airyscan of an OT-I CTL expressing LAMP1-EGFP (green) and phalloidin-stained to visualize actin (red), fixed 10 minutes after stimulation on anti-CD3-coated glass surfaces. Scale bar = 5μm. N=14 from three independent experiments.

Fig. 3. Removal of cortical actin permits secretion in CTLs. Time lapse TIRF images showing an OT-I CTL expressing LifeAct-mApple (gray scale, top rows), LAMP1-EGFP (gray scale, middle rows), and merged channels (bottom rows, LifeAct-mApple: red; LAMP1-EGFP: green) that have already secreted and recovered actin in response to anti-CD3-coated glass (-0:15), then treated at 0:00 with (A) 1μM Latrunculin A (LatA) or with (B) ethanol (EtOH), the carrier control. Degranulation event in (A) is highlighted by a yellow arrowhead. Kymographs of movies (right panels): fluorescence under a 5 pixel-thick region of interest (dashed white line) is displayed over time. Dashed yellow lines indicate time of treatment addition. Scale bar = 5μm in still TIRF images, scale bar = 2 minutes in kymographs. Time shown in minutes:seconds. (C) Graph depicts percent of cells that degranulated after treatment with carrier or LatA (mean ± SD). N=16 for carrier-treated cells; N=19 LatA-treated cells, from 3 independent experiments.

Fig. 4. Pharmacological inhibition of PLCγ inhibits actin clearance in CTLs. Representative spinning disk images of OT-I CTLs expressing LifeAct-mApple (red) and Tubby-EGFP (green) interacting with 1μM OVA_{257-26} peptide-pulsed EL4-Farnesyl-TagBFP2 target cells (blue) in the presence of (A) 1μM U-73343 inactive analog control (total N=175), (B) 1μM U-73122 PLCγ inhibitor (total N=184), or (C) 1μM U-73122 plus PMA and ionomycin (P/i) at 20ng/mL and 1μg/mL, respectively (total N=140). LifeAct-mApple and Tubby-EGFP channels are shown in gray scale. Scale bar = 5μm. Regions of fluorescence depletion indicated by yellow arrowheads.

(D) Graph depicts the percent of cells in conjugates with recovered actin (mean ± SD) from more than 3 independent experiments. **P<0.01 calculated by Student's T-test, ns=not significant.

Fig. 5. Ablation of PIP_2 at the membrane results in loss of cortical actin density and integrity. Representative TIRF images of Cos7 cells expressing (A) tagBFP2-FRB-PM, mRFP-5-ptase-FKBP12, and LifeAct-mEmerald, or (C) tagBFP2-FKBP12-PM, mRFP-5-ptase-FKBP12, and LifeAct-mEmerald, either before (left panels, i, iii, v) or after (right panels ii, iv, vii) Rapamycin treatment. Fluorescence signal from mRFP-5-ptase (top grayscale panels i, ii), LifeAct-mEmerald (middle grayscale panels iii, iv), and merged channels (bottom panels v, vi) are shown. Quantification of fluorescence intensity of mRFP-5-ptase (red line) and LifeAct-mEmerald (green line) during (B) PIP_2 ablation (N=14) or (D) control conditions (N=8) are shown. Black arrowheads indicate time of Rapamycin addition. Solid line is the mean of the data and shaded area indicates standard error. Dashed yellow lines (vi) highlight the area from which the intensity of the cell was measured. Scale bars = 10um.

Fig. 6. PIP_2 correlates with cortical actin density at the synapse. (A) Representative TIRF images of an OT-I CTL expressing LifeAct-mApple (red) and Tubby-EGFP (green) interacting with anti-CD3-coated glass (merge, bottom row). LifeAct (top row) and Tubby-EGFP (middle row) are shown in gray scale. Dashed yellow lines in i, ii indicate area from which line scans at (B) 0:48 and at (C) 2:32 are derived from, showing LifeAct (red) and Tubby-EGFP (green) intensities across the region of interest. N=11 cells from 4 independent experiments. Scale bars = 5μm. Time shown in minutes:seconds.

Fig. 7. Removal of recovered cortical actin does not affect PIP_2 at the synapse. (A) Time lapse TIRF images of an OT-I CTL expressing LifeAct-mApple (gray scale, top rows) and Tubby-EGFP (gray scale, middle rows), or merged channels (bottom rows) that have already secreted and recovered actin in response to anti-CD3-coated glass surfaces (-0:40), then treated at 0:00 with 1uM Latrunculin A. Kymographs of movies (right panels): fluorescence under a 3 pixel-thick region of interest (dashed white line) is displayed over time. Dashed yellow lines indicate time of treatment addition. Scale bar = 5μm; scale bar = 2 minutes in kymographs. Time shown in minutes:seconds. (B) Graph depicts percent of cells that with cleared reporter (LifeAct, red bars or PIP_2, green bars) at the membrane 3 minutes after treatment with carrier or Latrunculin A (mean ± SD). N=19 for carrier-treated cells; N=81 LatA-treated cells, from 3 independent experiments.

Fig. 8. Secretion-deficient *Rab27a*$^{ash/ash}$ CTLs show impaired actin recovery. Representative time lapse TIRF images and kymographs of (A) *Rab27a*$^{ash/ash}$ or (B) WT CTLs expressing LifeAct-mApple (red) and LAMP1-EGFP (green) interacting with anti-CD3-coated glass. Gray scale images for LifeAct (top rows) and LAMP1 (middle rows) are included; bottom rows show merged channels. A yellow arrowhead highlights degranulation event in WT panel. Kymographs of movies (right panels). Scale bar = 5μm in TIRF images, scale bar = 2 minutes in kymographs. Time shown in minutes:seconds. WT N=6 and *Rab27a*$^{ash/ash}$ N=9 from 3 three independent experiments. (C) Graph represents percent of WT (black bars) or *Rab27a*$^{ash/ash}$ (white bars) cells with recovered actin at 3 minutes and 8 minutes after interaction with anti-CD3-coated glass (mean ± SD). For 3 minute time point, WT N=1791 and *Rab27a*$^{ash/ash}$=1418. For 8 minute time point, WT N=3123 and *Rab27a*$^{ash/ash}$ =3054, both from 3 independent experiments. **P<0.01

calculated by Student's T-test, ns=not significant. (D) Graph represents percent of WT (black bars) or *Rab27a*$^{-/-}$ (white bars) cells with recovered PIP_2 at 3 minutes and 8 minutes after interaction with anti-CD3-coated glass (mean ± SD). For 3 minute time point, WT N=282 and *Rab27a*$^{-/-}$=299. For 8 minute time point, WT N=288 and *Rab27a*$^{-/-}$ =248. Actin and PIP_2 were quantitated from 2 different sets of 3 independent experiments. *$P<0.05$ calculated by Student's T-test, ns=not significant.

Supplementary Figure Legends

Fig. S1. Cortical actin recovers at the synapse during CTL:target interactions. Spinning disk confocal time lapse of an OT-I CTL expressing LifeAct-mEmerald (green) interacting with an EL4 target cell expressing TagRFP-MEM (red) pulsed with 1μM OVA_{257-26} (merge, bottom row, highlighted by dotted line). Images showing signal from the LifeAct (488) channel in a single slice correspond to the center of the synapse and are shown in gray scale (top row). Yellow arrowheads highlight area of reduced cortical actin density. Representative of N=11 cells from 3 independent experiments.

Fig. S2. 3D SIM of recovered actin and lytic granules at the synapse. (A) Representative 3D SIM projection of recovered cortical actin in a phalloidin-stained OT-I CTL fixed after 10 minutes following stimulation on anti-CD3-coated glass surfaces. (B) 3D SIM image rotated 90 degrees in the z plane to visualize actin (top panel, grayscale), LAMP1 (middle panel, grayscale), or merge (bottom panel) showing LAMP1+ granules on the cytosolic side of recovered cortical actin. Granules are highlighted by a yellow dotted line in the LAMP1 panel. Scale bars = 5μm.

Fig. S3. CTL function in U-73122-treated CTLs is rescued by PMA/ionomycin. Intracellular cytokine production is inhibited in U-73122-treated CTLs, but is rescued by PMA plus ionomycin treatment in the presence of the inhibitor. *In vitro* activated OT1 CTLs treated with either U-73122 or U-73433 control (both 1μM, final concentration) and stimulated for six hours with 5μg/mL plate-bound anti-CD3 or left un-stimulated as a control, +/- PMA (20ng/mL, final concentration) and ionomycin (1μg/mL, final concentration). Representative of two independent experiments.

Fig. S4. 5-phosphatase recruited by Rapamycin inducible dimer system reduces levels of PIP_2 in plasma membrane. (A) Schematic of inducible dimer system for the manipulation of plasma membrane-localized PIP_2. A cytosolic 5-phosphatase linked to mRFP is recruited to the PM by way of a Rapamycin-dependent heterodimerization of FKBP12 with membrane-bound FRB. (B) Representative TIRF images of COS7 cells expressing mRFP-FKBP12-5-ptase (i,ii), Tubby-EGFP (iii,iv), and tagBFP2-FRB-PM (not pictured) before treatment with Rapamycin (i,iii,v) and after treatment (ii,iv,vi). Merged before and after image shown in (v,vi). Scale bar = 10μm.

Fig S5. Carrier control experiment for Latrunculin treatment of LifeAct-mApple and Tubby-EGFP-expressing CTLs. (A) Time lapse TIRF images of an OT-I CTL expressing LifeAct-mApple (gray scale, top rows) and Tubby-EGFP (gray scale, middle rows), or merged channels (bottom rows) that have already secreted and recovered actin in response to anti-CD3-coated glass surfaces (-0:40), then treated at 0:00 with EtOH, the carrier control for Latrunculin A. Kymographs of movies (right panels): fluorescence under a 3 pixel-thick region of interest (dashed white line) is displayed over time. Dashed yellow lines indicate time of treatment addition. Scale bar = 5μm. Time shown in minutes:seconds.

Supplementary Movie Legends

Movie S1. Cortical actin recovers at the synapse following loss of membrane integrity in targets. Spinning disk movie showing a single slice through the center of the synapse of an OT-I CTL expressing LifeAct-mEmerald (left panel) interacting with a 1μM OVA_{257-26} peptide-pulsed EL4 labeled with GCaMP6m. Merged channel images shown in the right panel. Two-color images acquired every 10 seconds. Time shown in minutes:seconds. Scale bar = 10μm.

Movie S2. Cortical actin recovers at the synapse during CTL:target interactions. Spinning disk movie showing a single slice through the center of the synapse of an OT-I CTL expressing LifeAct-mEmerald (left panel) interacting with a 1μM OVA_{257-26} peptide-pulsed EL4 expressing tagRFP-MEM. Merged channel images shown in the right panel. Two-color images acquired every 5 seconds. Time shown in minutes:seconds. Scale bar = 5μm.

Movie S3. Cortical actin recovery in CTLs follows lytic granule secretion. TIRF movie of an OT-I CTL expressing LifeAct-mApple (left panel), and LAMP1-EGFP (center panel) interacting with glass coated with anti-CD3ε antibodies. Merged channel images shown in the right panel. Two-color images acquired every 2.4 seconds. Time shown in minutes:seconds. Scale bar = 5μm.

Movie S4. Recovered cortical actin forms a barrier behind which lytic granules are observed. 3D SIM movie of an OT-I CTL expressing LAMP1-EGFP (green) and stained with phalloidin to visualize actin (red) rotated in the z plane. Scale bar = 5μm.

Movie S5. Airyscan confocal moving through z stack. Successive 0.2μm z stack images obtained via Airyscan confocal imaging of an OT-I CTL expressing LAMP1-EGFP (green) and phalloidin-stained to visualize actin (red), fixed 10 minutes after stimulation on anti-CD3-coated glass surfaces. Scale bar = 5μm. N=14 from three independent experiments.

Movie S6. Removal of cortical actin following Latrunculin A treatment permits secretion in CTLs. TIRF movie of an OT-I CTL expressing LifeAct-mApple (left panel) and LAMP1-EGFP (center panel) interacting with glass coated with anti-CD3ε antibodies. Merged channel images shown in the right panel. Latrunculin A introduced at time 2:00. Two-color images acquired every 2.0 seconds. Time shown in minutes:seconds. Scale bar = 5μm.

Movie S7. Carrier control for Latrunculin A treatment has no effect on actin density and secretion in CTLs. TIRF movie of a WT CTL expressing LifeAct-mApple (left panel) and LAMP1-EGFP (center panel) interacting with glass coated with anti-CD3ε antibodies. Merged channel images shown in the right panel. Ethanol (carrier control for Latrunculin A) introduced at time 1:30. Two-color images acquired every 1.4 seconds. Time shown in minutes:seconds. Scale bar = 5μm.

Movie S8. Rapamycin-induced 5-ptase recruitment to the plasma membrane leads to reductions in PIP_2. TIRF movie of COS7 cells expressing Tubby-eGFP (left), FKBP12-5-ptase-mRFP (centre), and tagBFP2-FRB-PM (not pictured). Merged images shown in the right panel. Rapamycin is introduced to culture medium at 1:02. Images acquired on a 2.0 second interval, scale bar = 10μm.

Movie S9. Ablation of PIP_2 at the membrane results in loss of cortical actin density and integrity. TIRF movie of COS7 cell expressing Lifeact-mEmerald (left), FKBP12-5-ptase-mRFP (centre), and tagBFP2-FRB-PM (not pictured). Merged images displayed in the right panel. Rapamycin is introduced to culture medium at 5:00. Images acquired on a 50 second interval, scale bar = 10μm.

Movie S10. Control for PIP_2 ablation; Rapamycin treatment has no effect on actin density. TIRF movie of COS7 cell expressing Lifeact-mEmerald (left), FKBP12-5-ptase-mRFP (centre), and tagBFP2-FKBP-PM (not pictured). Merged images displayed in the right panel. Rapamycin is introduced to culture medium at 6:30. Images acquired on a 15 second interval, scale bar = 10μm.

Movie S11. PIP_2 clearance and recovery correlates with cortical actin density at the synapse. TIRF movie of a WT CTL expressing LifeAct-mApple (left panel) and Tubby-EGFP (center panel) interacting with glass coated with anti-CD3ε antibodies. Merged channel images shown in the right panel. Two-color images acquired every 4 seconds. Time shown in minutes:seconds. Scale bar: 5μm.

Movie S12. Removal of recovered cortical actin does not affect PIP_2 at the synapse. TIRF movie of an OT-I CTL expressing LifeAct-mApple (left panel) and Tubby-EGFP (center panel) interacting with glass coated with anti-CD3ε antibodies. Merged channel images shown in the right panel. Latrunculin A introduced at time 0:48. Two-color images acquired every 3 seconds. Time shown in minutes:seconds. Scale bar = 5μm.

Movie S13. Carrier control for Latrunculin A treatment has no effect on actin or PIP_2 in CTLs. TIRF movie of an OT-I CTL expressing LifeAct-mApple (left panel) and Tubby-EGFP (center panel) interacting with glass coated with anti-CD3ε antibodies. Merged channel images shown in the right panel. Ethanol (carrier control for Latrunculin A) introduced at time 1:12. Two-color images acquired every 3 seconds. Time shown in minutes:seconds. Scale bar = 5μm.

Movie S14. Secretion-deficient *Rab27a*$^{-/-}$ CTLs show impaired actin recovery. TIRF movie of a Rab27A-deficient CTL expressing LifeAct-mApple (left panel) and LAMP1-EGFP (center panel) interacting with glass coated with anti-CD3ε antibodies. Merged channel images shown in the right panel. Two-color images acquired every 2.1 seconds. Time shown in minutes:seconds. Scale bar = 5μm.

Movie S15. WT control CTLs for *Rab27a*$^{-/-}$ experiment secrete lytic granules and recover actin across the synapse. TIRF movie of a WT, secretion competent CTL expressing LifeAct-mApple (left panel) and LAMP1-EGFP (center panel) interacting with glass coated with anti-CD3ε antibodies. Merged channel images shown in the right frame. Two-color images acquired every 2.4 seconds. Time shown in minutes:seconds. Scale bar = 5μm.